Nano-engineered defect structures in Ce- and Ho-doped metal-organic chemical vapor deposited $YBa_2Cu_3O_{6+\delta}$ films: Correlation of structure and chemistry with flux pinning performance

T. Aytug,[1,a)] Z. Chen,[2] V. A. Maroni,[2] D. J. Miller,[2] C. Cantoni,[1] E. D. Specht,[1] A. J. Kropf,[2] N. Zaluzec,[2] Y. Zhang,[1] Y. Zuev,[1] and M. Paranthaman[1]
[1]*Oak Ridge National Laboratory, Oak Ridge, Tennessee 37831, USA*
[2]*Argonne National Laboratory, Argonne, Illinois 60439, USA*

(Received 7 February 2011; accepted 13 April 2011; published online 15 June 2011)

This study reports on the fabrication of metal-organic chemical vapor deposited (MOCVD) $YBa_2Cu_3O_{6+\delta}$ (YBCO) films doped with varying amounts of Ce and Ho and the characterization of their electrical, microstructural, and chemical properties. The films are prepared by vapor phase deposition of a Y-Ba-Cu precursor mix containing controlled amounts of Ce and Ho onto buffered metal strip templates. The comprehensive characterization of these films by critical current measurement, transmission electron microscopy, x-ray diffraction, Raman microspectroscopy, and x-ray absorption spectroscopy provides detailed information about the structure/chemistry/performance relationships and how they vary with varying amounts of Ce and Ho in the YBCO films. The microstructure exhibited by both the Ce-doped and the Ho-doped films contains a high density of crystal basal-plane aligned, fluoritelike precipitates within the YBCO matrix. For optimally doped samples, the influence of these nanocrystalline phases on the flux pinning properties manifests itself as a significant improvement in the critical current density (J_c) for magnetic field orientations that approach being parallel to the *ab* planes of the YBCO, while no appreciable change is observed in either self-field J_c or applied-field J_c performance in the vicinity of field orientations parallel to the YBCO *c*-axis. The Ce is almost exclusively concentrated in the fluoritelike nanoprecipitates, while the Ho incorporates into both the planar arrays of nanoprecipitates and the superconducting matrix, where it substitutes for Y in the YBCO lattice. The present findings for Ce and Ho doping are in interesting contrast with our prior findings for Zr-doped MOCVD films due to the fact that the Zr-doped films exhibit columnar precipitate arrays that produce a substantial improvement in J_c for magnetic field orientations parallel to the YBCO *c*-axis, while no appreciable change is observed in either self-field or applied-field J_c performance for field orientations parallel to the *ab* planes. These results suggest that improvement of the in-field J_c of YBCO films over an extended range of field angles could be achieved by doping strategies that simultaneously produce both *ab*-plane aligned and *c*-axis aligned precipitate arrays.
 [doi:10.1063/1.3592244]

I. INTRODUCTION

Films of $REBa_2Cu_3O_{6+\delta}$ (REBCO, RE = Y or a rare earth metal) deposited on long-length, metal tapes with cube textured surfaces are at the forefront for applications of superconducting wire in electric power applications.[1–5] In this same context, metal-organic chemical vapor deposited (MOCVD) film growth methodologies are particularly well suited for industrial-scale wire production.[5] Significant advances in the electrical performance and length scale of MOCVD-based coated conductors (CCs) have been made in recent years.[1,5] REBCO CCs in kilometer lengths that carry critical currents (I_c) approaching 300 A per centimeter width (A/cm-w) have been manufactured. Also, on a research and development scale, I_c values exceeding 800 A/cm-w in meter-length wire specimens have been achieved.[1,5] While these are impressive results, the performance target for economically tenable, long-length CCs is 1000 A/cm-w in lengths exceeding a kilometer.[6] Two pathways are being explored to reach this target. One is to fabricate progressively thicker REBCO films that retain the same through-thickness critical current density, J_c, exhibited by the 1- to 2-μm-thick REBCO films currently being produced. The second is to raise J_c by increasing the strength of the intrinsic and extrinsic flux pinning in the MOCVD REBCO. In this same context, there is also considerable incentive to optimize the flux pinning landscape in ways that lead to a more uniform angular dependence of the in-field J_c. In recent years, several groups have reported on the enhancement of flux pinning in MOCVD REBCO films through the incorporation of nanoscale structures in the REBCO matrix.[7–16]

In this paper, we present the results of studies devoted to (1) characterization of the phase chemistry and microstructure of REBCO films (RE = Y) produced by MOCVD processing using a precursor mix containing varying mole percentages (mol. %) of added Ce and Ho, (2) correlation of this chemical and microstructural information with electrical performance

a)Author to whom correspondence should be addressed. Electronic mail: aytugt@ornl.gov.

properties of the metal-doped YBCO films in an applied magnetic field, and (3) comparison of these results with our prior work on Zr-doped MOCVD YBCO.[7,8] The template employed as a substrate for these MOCVD YBCO films is the one currently used by SuperPower, Inc. for their long length, MOCVD-based CC.[1] We apply a combination of transmission electron microscopy (TEM), energy dispersive spectroscopy (EDS), x-ray diffraction (XRD), Raman microspectroscopy, and x-ray absorption spectroscopy (XAS) methods to obtain information about (1) nanoscale features embedded in the YBCO matrix, (2) the relative amounts of nonsuperconducting second phases, including phases containing the additive elements (Ce and Ho), and (3) YBCO texture quality and lattice disorder. Evidence of differences in current carrying performance, phase chemistry, and microstructural features resulting from the fact that Ho freely enters the YBCO lattice but Ce does not is presented and discussed.

II. EXPERIMENTAL

A custom-designed vertical, cold-wall, reel-to-reel MOCVD apparatus based on a liquid-source delivery system was used to prepare the YBCO films on $LaMnO_3$/IBAD-MgO templates. The process technology employed by SuperPower, Inc. to produce these templates has been discussed elsewhere.[17] The details of the prototype MOCVD system are reported in Refs. 18 and 19. In essence, a single source liquid was prepared by dissolving solid metal-organic precursors (specifically, the Y, Ba, Cu, Ce, and Ho salts of 2,2,6,6-tetramethylheptanedionate) in tetrahydrofuran with appropriately formulated molar ratios. The Y:Ba:Cu mole ratio was fixed at 1.3:2:2.6. The Ce or Ho was added to the YBCO precursor mix in amounts ranging from 1 to 20 mol. % relative to the Y content. This solution was then transferred to the vaporizer by a liquid pump. The resulting vapors were carried by argon gas and mixed with oxygen before being injected into a showerhead above the continuously moving heated substrate (moving at a rate of ~150 cm/h) to produce the 0.4 to 0.6 μm thick YBCO films examined in this work. The pressure in the reactor was adjusted to 2.5 Torr and the radiant heater temperature was maintained near 950 °C. This procedure enabled the study of variations/trends in the structural properties and superconducting performance of YBCO films with respect to Ce or Ho content.

The electrical properties (T_c and J_c) of the fully processed films were measured using a standard four-probe technique, with values of J_c assigned using a 1 μV/cm criterion. The angular dependence studies were performed at 77 K in a 1 T field that was oriented at various angles with respect to the tape normal over a range of 180°, in the full Lorentz force configuration.

Cross-sectional TEM examinations were conducted using a Philips CM200 TEM-Scanning TEM microscope equipped with a 200 kV field-emission gun, an EDAX R-TEM Si(Li) energy dispersive spectroscopy detector, and an Emispec Vision acquisition system. The Z-contrast images were recorded using a Fischione high angle annular dark field detector. X-ray spectral images were acquired with a probe size of 1.5 nm and a step length of 2 nm. The elemental maps were obtained by plotting the integrated intensities of characteristic x-ray peaks for each spectrum after background subtraction.

The crystallography and phase content of the Ce- and Ho-doped films were analyzed by XRD. The θ-2θ scans were measured in the Bragg-Brentano geometry using a Cu source operating at 50 kV and 100 mA and a Peltier-cooled energy-dispersive Si(Li) detector tuned to Cu Kα. The samples were tilted for alignment with the YBCO (00L) reflections. Crystallographic phase and texture were analyzed using a 4-circle x-ray diffractometer employing the same Cu source and a bent graphite monochromator tuned to Cu Kα. The diffracted beam was collimated using 0.5° Soller slits upstream of a NaI scintillation detector. The integrated peak intensity, E, of the Bragg reflection with reciprocal lattice vector, HKL, is given by the following proportional relationship,[20]

$$E \sim \frac{V|F_{HKL}|\lambda^2}{v^2} \cdot \left(1 + \cos^2 2\theta\right), \tag{1}$$

where V is the volume of the phase or texture component, F_{HKL} is the structure factor, v is the unit cell volume, λ is the wavelength, and 2θ is the Bragg angle. The integrated intensity is given by

$$E = \int Idq = \frac{\lambda^3}{\sin^2\theta\cos\theta\cos\chi}\int Id(2\theta)d\chi d\phi \sim \frac{\lambda^3 I_0}{\sin^2\theta\cos\theta\cos\chi}\Delta(2\theta)\Delta\chi\Delta\phi, \tag{2}$$

where q is the scattering vector and χ and ϕ are diffractometer angles.[21] D(2θ), Dχ, and $\Delta\phi$ are the full with at half maximum of Gaussian fits to scans through the peak; I_0 is the peak intensity. The volume fraction is found by combining Eqs. (1) and (2):

$$V \sim \frac{v^2 I_0 \Delta(2\theta)\Delta\chi\Delta\phi}{|F_{HKL}^2|\sin^2\theta\cos\theta\cos\chi(1+\cos^2 2\theta)}. \tag{3}$$

Parameters for the phase volume fraction calculations are listed in Table I. The phases are taken to be $YBa_2Cu_3O_7$ and Y_2O_3 for the calculation.

Raman spectroscopy was used to gauge texture quality, detect and quantify lattice disorder effects, and probe for Cu-rich second phases (e.g., CuO and barium cuprates). Raman spectra were recorded using a Renishaw InVia Raman

TABLE I. Parameters for the volume fraction calculation.

Phase	Reflection HKL	Unit cell volume v	Structure factor F_{HKL}	Reference
YBCO	(103)/(013)	174	164	[a]
Y_2O_3	(222)	1194	954	[b]

[a]R.M. Hazen, L.W. Finger, R.J. Angel, C.T. Prewitt, N.L. Ross, H.K. Mao, C.G. Hadidiacos, P.H. Hor, R.L. Meng, and C.W. Chu, Phys. Rev. B **35**, 7238 (1987).
[b]C. Santos, K. Strecker, P.A. Suzuki, S. Kycia, O.M. M. Silva, and C. R. M. Silva, Mater. Res. Bull. **40**, 1094 (2005).

Microprobe equipped with a 633 nm He-Ne laser. The laser power density was maintained at a level well below 1 mW/μm^2 to prevent thermal damage to the YBCO films. The sample handling and spectra processing procedures employed in this work have been discussed in prior publications.[22,23] The through-thickness Raman measurements were facilitated by milling a surface-to-substrate crater through each YBCO film. This crater provided a tapered through-thickness slope along which the Raman spectra were collected. The method used to produce the tapered slope is discussed in Ref. 8. All Raman spectra were recorded at ambient temperature.

X-ray absorption spectroscopy measurements in the Ho L3 edge region were made on MRCAT beamlines 10ID and 10BM at Argonne's Advanced Photon Source. Both beamlines used double-crystal Si(111) monochromators to select the incident x-ray photon energy. On 10ID, harmonic rejection was obtained using a Rh-coated mirror and on 10BM harmonic rejection was accomplished with 50% detuning. The beam was incident upon the thin-film samples at a low angle (between 2 and 3°) to minimize the background signal from the substrate. The Ho fluorescence was detected using Soller slits, a 3-absorption-length Fe filter (EXAFS Materials), and a large area ionization chamber (Ar gas, 270 V, The EXAFS Company).

III. RESULTS

Dopant levels, critical temperatures, and electrical performance properties for representative Ce- and Ho-doped MOCVD YBCO samples reported upon in this paper are listed in Table II together with previously reported results for an optimized Zr-doped MOCVD YBCO sample.[7,8] For all of the samples listed in Table II we note that the Y:Ba:Cu stoichiometry of the precursor solution delivered to the showerhead was held at the ratio 1.3:2.0:2.6 as the dopant element was added. This particular Y:Ba:Cu stoichiometry is chosen based on the MOCVD reactor optimization runs that showed (1) Ba:Cu = 2:2.6 produces the desired balance of Ba and Cu in the superconducting phase, and (2) the slightly over-stoichiometric Y content (1.3) drives the nonsuperconducting phase mix toward the fluorite phase (RE_2O_3) which tends to form as nanoscale precipitates that reportedly facilitate flux pinning (see, e.g., Ref. 9 and references therein).

TABLE II. Summary of superconducting properties for an undoped MOCVD YBCO film and for the Ce- and Ho-doped MOCVD YBCO films.

Film composition	T_c (K)	J_c (77 K, self-field) (MA/cm^2)	J_c//c (77 K, 1 T) (MA/cm^2)	J_c//ab (77 K, 1 T) (MA/cm^2)
Undoped YBCO	89.7	1.8	0.19	0.44
Zr (5mol. %) [7]	89.1	1.8	0.30	0.44
Ce (2.5mol. %)	90.8	1.9	0.17	0.60
Ce (5mol. %)	90.5	2.0	0.21	0.98
Ce (10mol. %)	89.6	1.1	0.01	0.15
Ho (2.5mol. %)	89.6	1.8	0.14	0.58
Ho (5mol. %)	89.3	1.8	0.18	0.72
Ho (10mol. %)	88.7	1.8	0.18	0.94
Ho (20mol. %)	88.9	1.0	0.08	0.30

The nominal YBCO film thickness values for the Ce- and Ho-doped samples were in the range of 0.4 to 0.6 μm.

A. Critical current characterization

It can be seen from the superconducting critical temperature (T_c) values in Table II that doping with Ce and Ho (and Zr as well) has very little effect on the critical temperature of the YBCO for all doping levels reported here. Doping with these elements also has relatively little effect on the critical current density, J_c, at 77 K, self-field, except at the highest doping levels in the case of Ce and Ho. Figures 1(a) and 1(b) show the dependence of J_c on the applied magnetic field (H) angle for the Ce- and Ho-doped samples, respectively. For both Ce and Ho the most pronounced effect of the doping is seen around H//ab. In the case of Ce doping, the enhanced pinning around H//ab increases with an increasing Ce addition up to Ce = 5 mol. % then decreases sharply with the increasing Ce addition. At 5 mol. % Ce the J_c at H//ab is over a factor of two higher than that for undoped YBCO. In the case of Ho doping, a similar enhancement is seen around H//ab; this enhancement peaks at 10 mol. % Ho, and J_c at the composition of maximum enhancement (10 mol. % Ho) is again twice as high as that of the undoped YBCO film.

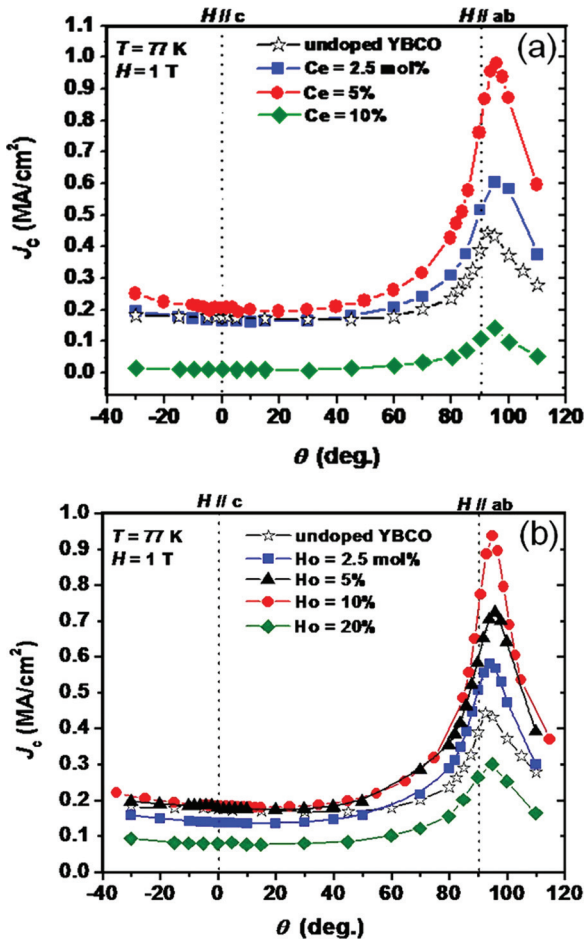

FIG. 1. (Color online) Dependence of J_c on orientation angle of the field relative to the c-axis direction (maximum Lorentz force configuration) for films modified with various concentrations of (a) Ce and (b) Ho that display a substantial increase in J_c for fields aligned near ab-planes relative to undoped YBCO films.

However, there is no evidence of a significant increase in J_c in the vicinity of $H//c$ or in the minimum J_c underlying the entire angular range (referred to hereinafter as the "floor"). Also, at doping levels beyond where the J_c maxima occur for Ce and Ho additions, the "floor" J_c appears to be dropping off along with the $H//ab$ pinning.

B. Electron microscopy

Figure 2 presents TEM images for (a) 5 mol. % Ce in YBCO, (b) 10 mol. % Ho in YBCO, and (c) 20 mol. % Ho in YBCO. Both the Ce and the Ho-doped films show clear evidence of correlated planar defects composed of arrays of nanoprecipitates. As the additive concentration of Ce or Ho is increased, the nanoprecipitates tend to agglomerate and the planar arrays tend to thicken. This can be seen by the comparison of the images in Figs. 2(b) and 2(c) for the 10 and 20 mol. % Ho films, respectively.

The high resolution TEM image of the 5 mol. % Ce film in Fig. 3(a) reveals the presence of numerous stacking faults and short antiphase boundaries (APBs) surrounding each single precipitate in the plate arrays. The image was acquired with the zone axis along YBCO [010] and shows an epitaxial relationship between the YBCO lattice and the cubic lattice of the precipitates. Figure 3(b) represents a low-frequency filtered image of Fig. 2(a), highlighting the change in the periodicity of the YBCO lattice planes due to the presence of stacking faults and other defects. Some of the most common stacking defects are indicated by white arrows and correspond to the insertion of additional CuO chains which provide the physical basis for the stacking fault structures in MOCVD films.[24] These structures sometimes appear as 124 stacking faults and have a periodicity of 13.3 Å (as opposed to 11.7 Å, which is the YBCO c-axis spacing). Note that as the YBCO planes of different sub-grains fail to fit together,

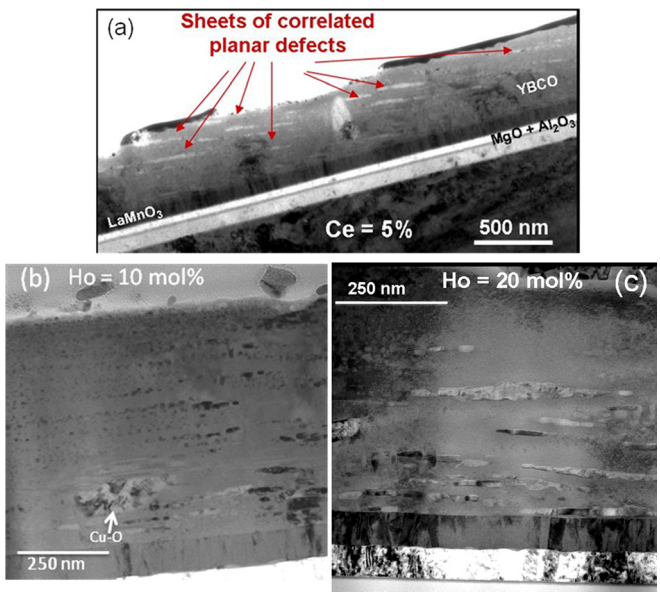

FIG. 2. (Color online) Cross-sectional TEM images of optimally doped YBCO films containing (a) 5 mol. % Ce, (b) 10 mol. % Ho, and (c) 20 mol. % Ho that illustrate the presence of high density precipitates mostly organized along the *ab*-planes.

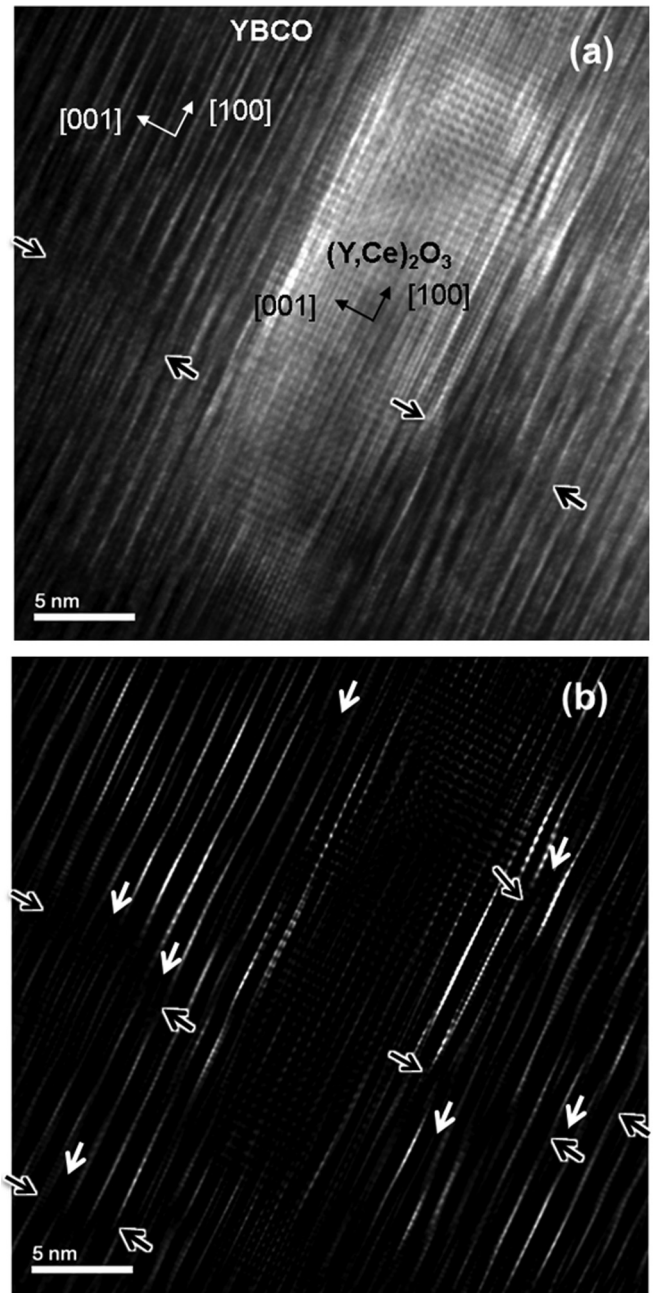

FIG. 3. (a) Cross-sectional high-resolution TEM and (b) low-frequency filtered images of the same sample as presented in Fig. 2(a), showing a $(Y,Ce)_2O_3$ nanoplate defect, along with some of the stacking faults (white arrows) and antiphase boundaries (black arrows) associated with the platelet. The disruption and bending of the lattice fringes, which are evident from image (b), clearly indicate the presence of various defects within the YBCO matrix surrounding the platelike nanoprecipitates.

APBs (indicated by double black arrows) form above and below the particles and might act as additional localized pinning centers and contribute to the observed enhancement in J_c around $H//ab$.[24]

Figures 4(a) through 4(d) show Y, Ce, Ba, and Cu spectral images, respectively, obtained from a representative region of the 10 mol. % Ce sample. The domains where Ba and Cu are dominant are known to comprise the YBCO matrix, while the domains where Ce and Y seem dominant are correlated with the locations of the nanoprecipitates. These

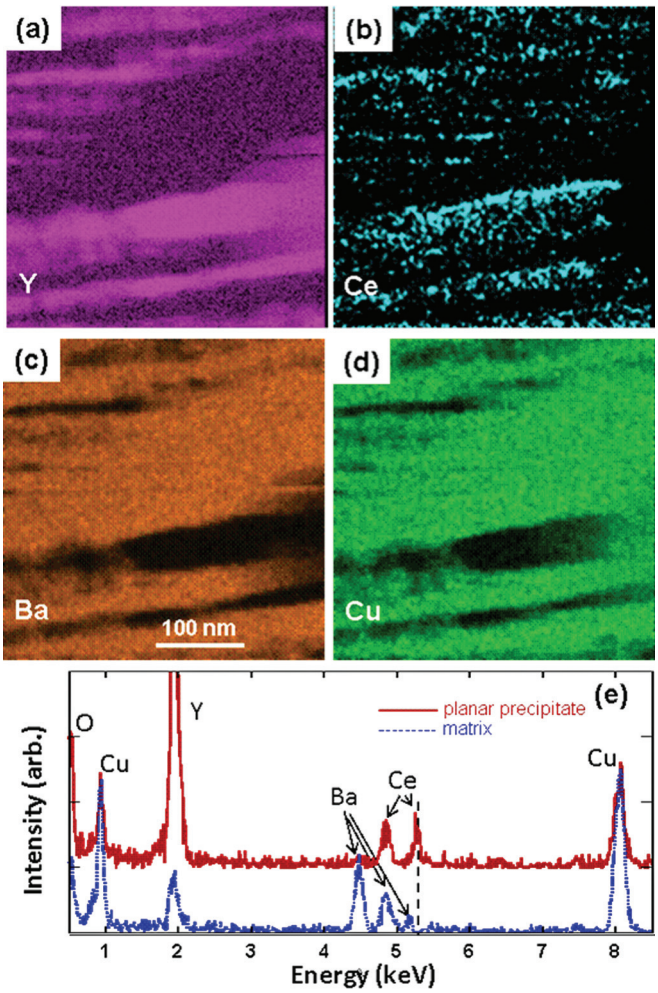

FIG. 4. (Color online) Images (a) through (d) show Y, Ce, Ba, and Cu spectral maps, respectively, taken over a representative domain of the 10 mol. % Ce-added YBCO film. (e) Displays the averaged EDS spectra obtained on the planar precipitates and YBCO matrix. The maps, along with the EDS spectra, reveal that the Ce is mainly incorporated in the nanoprecipitate arrays. The scale bar in inset (c) applies to all four maps.

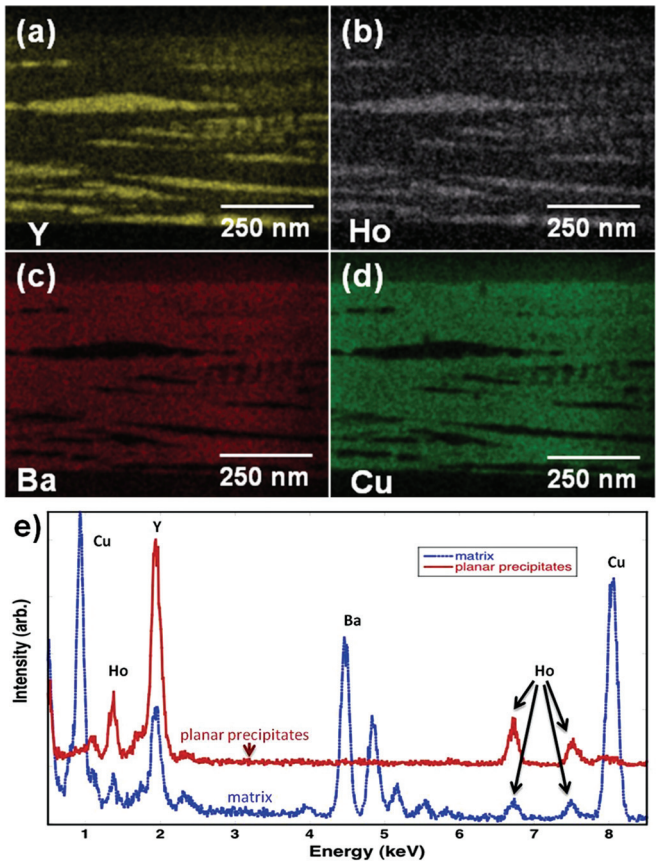

FIG. 5. (Color online) Images (a) through (d) show Y, Ce, Ba, and Cu spectral maps, respectively, taken over a representative domain of the Ho-added YBCO film. (e) Shows the averaged EDS spectra obtained on the planar precipitates and YBCO matrix. The maps and the EDS spectra reveal that the added Ho incorporates into both the planar precipitates and the YBCO matrix.

images indicate that (1) Ce is clearly concentrated in the precipitates, (2) Y is also enhanced in the precipitates, and (3) the precipitates seemingly contain no detectable Ba or Cu. Figure 4(e) shows averaged EDS spectra of Ce-rich and Ba-rich domains of this same film. Since the Ba-rich domains are known to be correlated with the YBCO matrix, it seems abundantly clear that there is very little Ce in the YBCO phase. This overall finding is consistent with the presence of a fluoritelike Y-Ce-O precipitate phase as discussed next.

The Y, Ce, Ba, and Cu spectral images from a representative region of the 20 mol. % Ho sample shown in Figs. 5(a) through 5(d) give evidence that the precipitates in the planar arrays are an Y-Ho-containing phase that is relatively free of Ba and Cu. Again, we surmise at this point, and will later show, that these precipitates are an $(Y,Ho)_2O_3$ phase with the expected fluoritelike lattice structure. Comparison of the Y and Ho images in Figs. 5(a) and 5(b), respectively, also indicates that some Ho is present in the YBCO matrix, which is not surprising considering that Ho reportedly substitutes freely on the Y site of YBCO.[25,26] Figure 5(e) shows averaged EDS spectra of domains that are rich in Y and Ho and other domains that are Ba-rich for this same film. These spectra reveal the presence of Ho in both the precipitates and the YBCO matrix. As in the case of the Ce doped films, the results are consistent with the presence of an Y-Ho-O precipitate phase that is relatively free of Ba and Cu.

C. XRD measurements

The XRD patterns for the 5 mol. % Ce added and 5 mol. % Ho added films shown in Figs. 6(a) and 6(b), respectively, are representative of the patterns for all the MOCVD YBCO films reported upon herein. These patterns reveal clear evidence for the formation of M_2O_3 type fluorite phases, where M is Ce + Y or Ho + Y. No significant formation of perovskite like phases was observed in the XRD patterns of any of the Ce- or Ho-doped films. In the case of the Ce-doped films, a particularly important finding is the absence of XRD evidence for $BaCeO_3$ or CeO_2 in the YBCO matrix. Instead, fluorite like phases having lattice parameters [0.5305 ± 0.00084 nm (mean ± standard deviation)] consistent with pure Y_2O_3 (0.5284 nm) were found to form with a volume fraction that is correlated with the level of RE-doping as shown in Fig. 7. The fluorite x-ray particle size was in the range 17 ± 2 nm, where the variation is consistent with experimental uncertainty.

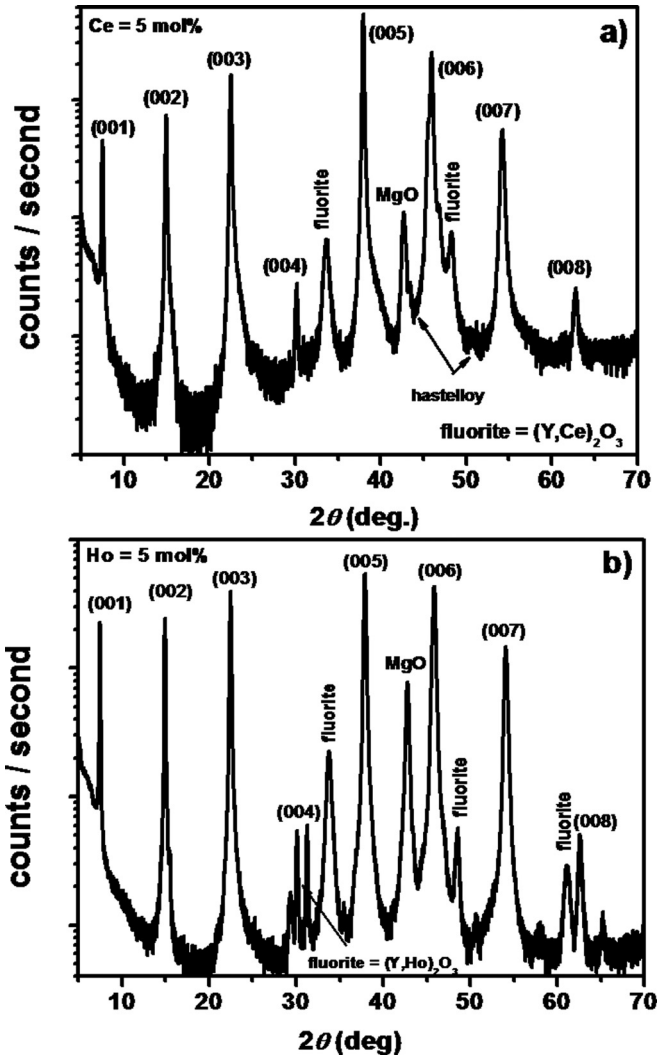

FIG. 6. XRD patterns of YBCO films with (a) 5 mol. % Ce and (b) 5 mol. % Ho additions. Scans indicate formation of fluorite (RE_2O_3) phases along with *c*-axis growth of YBCO.

Finally, large deviations in YBCO texture are observed at high doping levels. In addition to the dominant (001) ⟨100⟩ texture, the 10 mol. % Ce-doped film contains 5% (001)⟨110⟩ (rotated 45° in-plane), while the 10 and 20 mol. % Ho-doped films contain up to 9% (001)⟨110⟩ and 10% {100}[001] (*a*-axis normal).

D. Raman measurements

Raman measurements for all the films reported upon herein were performed by through-thickness examination, wherein a crater was milled into the YBCO film to form a sloped surface from the top of the film to the substrate. The overall approach was the same as that described in Ref. 8. A representative spectrum of each film was obtained by averaging spectra recorded at six to eight positions along each through-thickness slope. Averaged Raman spectra for undoped YBCO and for the 2.5, 5, and 10 mol. % Ce films are shown in Fig. 8. All spectral intensities were normalized to the O2 +/O3 − mode of YBCO at ~330 cm^{-1} to provide a means of gauging variations in spectral features associated with lattice disorder, second phases, etc. For the MOCVD

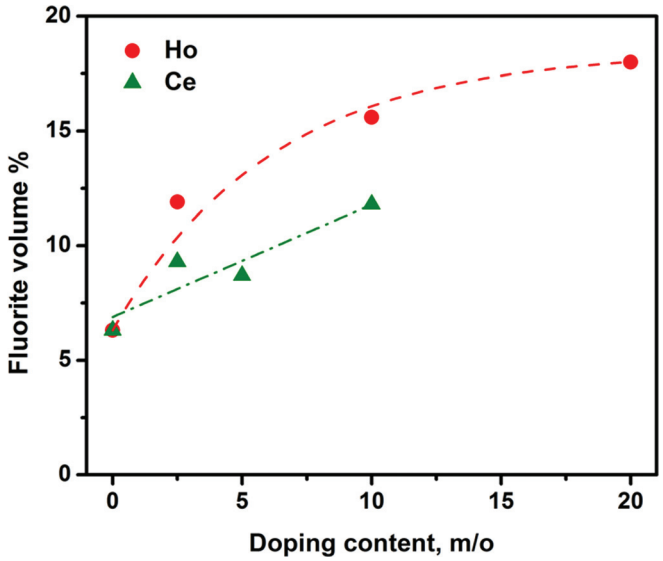

FIG. 7. (Color online) XRD determined fluorite phase fraction as a function of Ce and Ho doping levels. Dashed lines are intended to serve as a guide to the eye.

processing conditions used in this study, the YBCO films exiting the deposition chamber are under-doped in oxygen and the YBCO is in the tetragonal state (the phonons attributable to tetragonal YBCO are indicated with diamonds in Fig. 8). The results in Fig. 8 show: (1) that the band associated with cation disorder (C-Dis) in the YBCO lattice increases with increasing Ce addition and (2) that the Ce addition seems to cause a step increase in the barium cuprate phase content (Ba-Cu-O).[8,22] The overall effect of the Ce addition on C-Dis and Ba-Cu-O is highlighted by the spectral subtraction curve at the bottom of the plot, where we plot the difference spectrum obtained by subtracting the normalized spectrum of the undoped YBCO film from that of the 5 mol. %

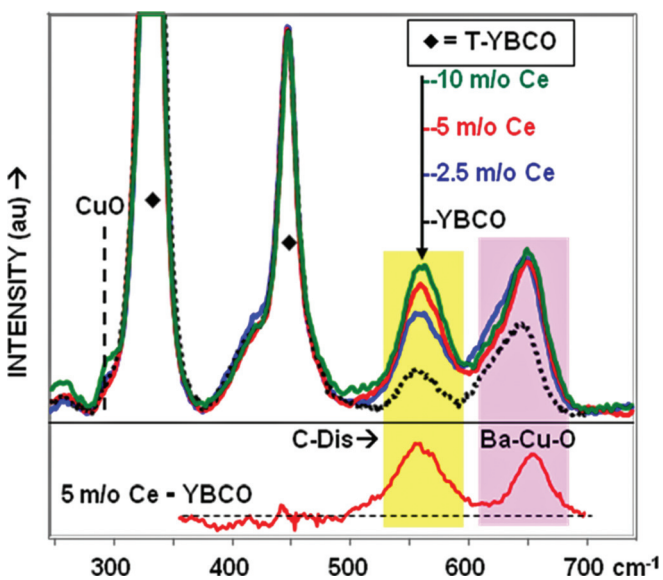

FIG. 8. (Color online) Normalized, averaged through-thickness Raman spectra of YBCO films doped with 2.5, 5, and 10 mol. % Ce. The typical Raman spectrum of an undoped MOCVD-YBCO film is also included for comparison. The bottom inset shows the results of subtraction of the undoped YBCO film spectrum from that of the 5 mol. % Ce-added film.

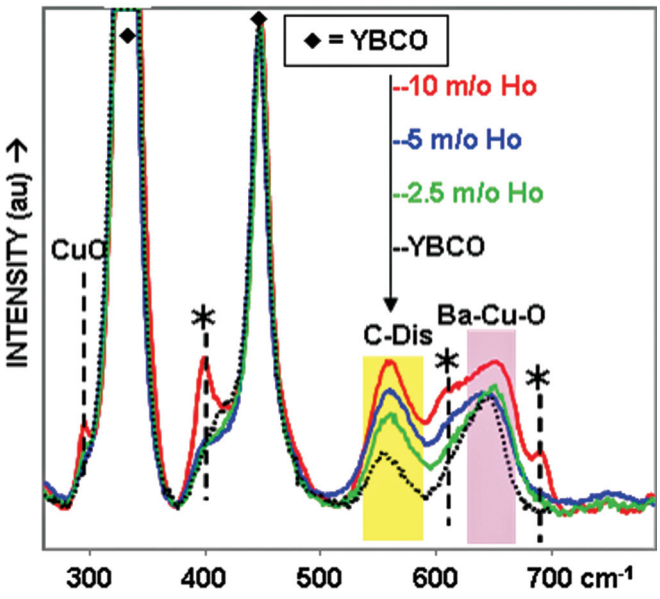

FIG. 9. (Color online) Comparison of the normalized, averaged through-thickness Raman spectra for the 2.5, 5, and 10 mol. % Ho-added samples together with the spectrum of an undoped MOCVD-YBCO film. Laser induced luminescence bands associated with Ho(III) in the fluorite phase lattice positions are highlighted with asterisks.

Ce added film. Furthermore, at the highest Ce doping level, evidence for the onset of CuO formation begins to appear in the Raman spectra as well ($\sim$300 cm^{-1}).

Figure 9 presents the normalized Raman spectra for the 2.5, 5, and 10 mol. % Ho added films together with the spectrum of undoped YBCO for comparison. In the case of Ho doping, accurate gauging of the cation disorder and Ba-Cu-O phase content is complicated by the presence of luminescence bands associated with Ho(III) in fluorite phase lattice positions. (Some of these luminescence bands are marked with asterisks in Fig. 9.) This effect is illustrated more clearly in Fig. 10 where we show the Raman spectrum of 20 mol. % Ho-doped YBCO (bottom trace), the luminescence spectrum of Ho in Ho_2O_3 (middle trace) induced by 633 nm laser excitation, and the Raman spectrum of a specially prepared MOCVD film (top trace) composed of $Ho_{0.5}Y_{0.5}Ba_2Cu_3O_{6+X}$ (i.e., REBCO with no excess RE to form RE_2O_3). Note the more pronounced presence of the Ho(III) luminescence in the 20 mol. % Ho added film as compared to the $Ho_{0.5}Y_{0.5}Ba_2Cu_3O_{6+X}$ film. This is due to the fact that the precursor stoichiometry for the 20 mol. % Ho film is richer in total Ho + Y compared to the precursor stoichiometry of the $Ho_{0.5}Y_{0.5}Ba_2Cu_3O_{6+X}$ film, which should produce a greater quantity of $(Y,Ho)_2O_3$ in the 20 mol. % Ho film. More significantly, the results in Fig. 10 provide further definitive evidence for the presence of Ho-containing fluorite phase precipitates in the Ho-doped films.

The effect of Ho doping on the CuO and Ba-Cu-O content of the MOCVD YBCO films can also be seen in Figs. 9 and 10. At the higher Ho levels, CuO ($\sim$300 cm^{-1}) clearly increases relative to undoped YBCO. Even though the Ho(III) luminescence complicates a definitive interpretation of the Ba-Cu-O mode behavior in Fig. 10, it appears that the relative amount of barium cuprates in Ho-doped and undoped YBCO are not much different.

Normalized Raman spectra of the best performing Ce-, Ho-, and Zr-doped films are illustrated in Fig. 11. (Here, the Zr results from Ref. 8 are included for purposes of comparison.) Since Ce ties up Y in the fluorite phase, it is not surprising that the Ba-rich (Ba-Cu-O) phase content tends to increase (relative to undoped YBCO) when Ce is added to the MOCVD precursor. For the Ho addition, if one considers that a portion of the aggregate intensity in the spectral region of interest (500 to 700 cm^{-1}) is contributed by the Ho(III) luminescence bands, it appears that the 10 mol. % Ho addition to YBCO induces somewhat less cation disorder than 5 mol. % Ce and 5 mol. % Zr and less Ba-Cu-O than 5 mol. % Ce. Also, $BaCeO_3$ does have a Raman active phonon centered near 350 cm^{-1}. However, no evidence of a distinct Raman band at this frequency is apparent along the side of the intense 330 cm^{-1} mode of YBCO in, for example, the spectrum of the 10 mol. % Ce film in Fig. 8. Similarly, CeO_2 has a characteristic Raman active phonon at 466 cm^{-1} but there

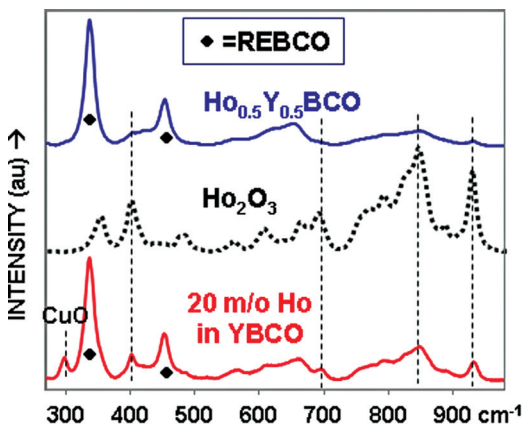

FIG. 10. (Color online) Comparison of the averaged through-thickness Raman spectra of the 20 mol. % Ho-added YBCO film and the $Ho_{0.5}Y_{0.5}Ba_2Cu_3O_{6+X}$ film with the 633-nm-excited luminescence spectrum of Ho in the Ho_2O_3 standard.

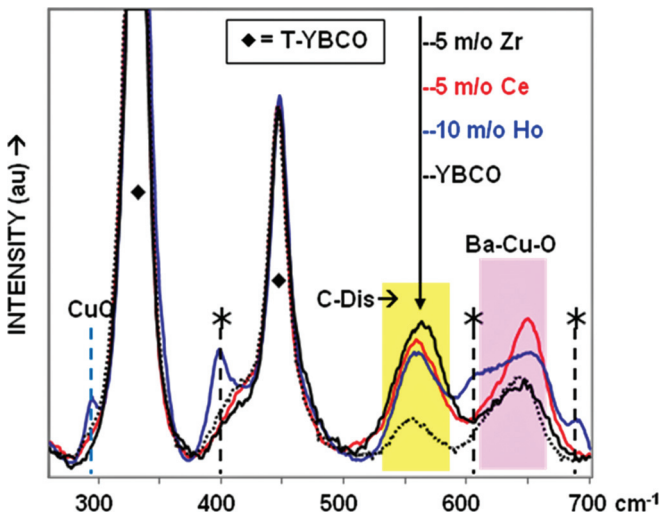

FIG. 11. (Color online) Normalized Raman spectra of optimally doped Ce- and Ho-added MOCVD YBCO films (i.e., 5 mol. % Ce and 10 mol. % Ho). The results are displayed together with the spectrum of an optimally doped Zr-added MOCVD film (i.e., 5 mol. % Zr).

is no evidence of a discernible feature on the high frequency side of the intense 450 cm^{-1} mode of tetragonal YBCO for any of the spectra in Fig. 8. So, to some extent, the Raman spectra are in agreement with the XRD results that neither $BaCeO_3$ nor CeO_2 is a prominent Ce-containing phase in the Ce-doped films.

E. XAS measurements

The synchrotron-based x-ray absorption spectral measurements provide information about the Ho oxidation state and likely Ho-containing phases. The normalized x-ray absorption spectra (i.e., normalized to a single Ho atom) for the entire series of Ho-doped films, for the $Ho_{0.5}Y_{0.5}Ba_2Cu_3O_{6+x}$ film, and for Ho_2O_3 powder are plotted in Fig. 12(a). In this measurement the Ho_2O_3 serves as both a phase standard and a Ho(III) oxidation state standard. Not surprisingly, the Ho in the YBCO films is clearly in the +3 state. Also, the isosbestic crossings [indicated by the three circles in Fig. 12(a)] appear to embrace the absorption curves for the four Ho-added films and Ho_2O_3, which is consistent with the premise that Ho in a fluorite lattice is one of the contributing phases to the absorption spectrum for each of the four Ho-added films. We note here that the absorption spectrum of the $Ho_{0.5}Y_{0.5}Ba_2Cu_3O_{6+x}$ film in Fig. 12(a) actually does not show the same isosbestic behavior as the spectra of the four Ho-added films and Ho_2O_3, most probably because the Ho/Y, (Ho + Y)/Ba, and (Ho + Y)/Cu atomic ratios are considerably different from those of the four Ho-added films. Furthermore, the normalized absorbance mismatch between the Ho_2O_3 spectrum and the spectra of the (Ho,Y)BCO films gives an additional strong indication that there are at least two Ho-containing phases contributing to the absorption spectra of the Ho-added films.

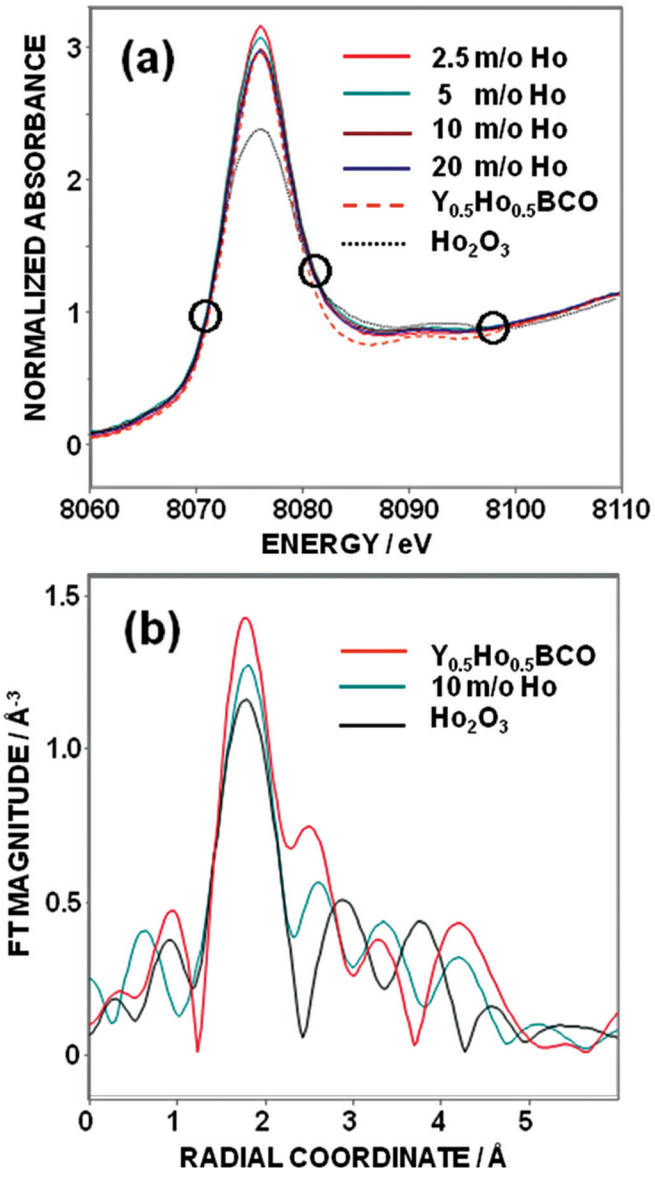

FIG. 12. (Color online) (a) Normalized x-ray absorption spectra in the Ho L3 edge region for the 2.5, 5, 10, and 20 mol. % Ho-added films and the Ho_2O_3 standard. The spectrum for the $Ho_{0.5}Y_{0.5}Ba_2Cu_3O_{6+x}$ film is also included for comparison. (b) EXAFS Fourier transforms (radial coordinate plots) for the 10 mol. % Ho-added film, the $Ho_{0.5}Y_{0.5}Ba_2Cu_3O_{6+x}$ film, and the Ho_2O_3 standard.

Plots of the Fourier transform (FT) magnitude derived from the extended x-ray absorption fine structure (EXAFS) results for the $Ho_{0.5}Y_{0.5}Ba_2Cu_3O_{6+x}$ film, the 10 mol. % Ho-added film, and the Ho_2O_3 powder are given in Fig. 12(b). In a qualitative sense, the match of the FT magnitude versus r curves for the $Ho_{0.5}Y_{0.5}Ba_2Cu_3O_{6+x}$ film and the 10 mol. % Ho-added film out to the second shell region indicates some structural similarity of the Ho-containing phase assemblage in each film. This similarity is even more pronounced for both the real and the imaginary components of the FT (not shown). The results in Fig. 12(b) give some indication that the mixing of appropriate standards for (Y,Ho)BCO and $(Y,Ho)_2O_3$, i.e., with each component of the standard having a Ho/Y ratio equivalent to that of the corresponding Ho-containing MOCVD film, would provide a match (in terms of both phase and FT magnitude) to the EXAFS data for each of the Ho-doped YBCO films. However, a tedious endeavor of that magnitude would add little to what we already know.

IV. DISCUSSION

The results of pinning enhancement reported herein for Ce and Ho additions to MOCVD YBCO provide an interesting dichotomy with our previously published results for Zr-doped MOCVD YBCO.[7,8] This dichotomy is illustrated in Fig. 13 which presents the J_c versus angle (θ) measurements (77 K, 1 T) for undoped MOCVD YBCO, the optimally doped Ce and Ho films previously discussed, and the optimally doped Zr film described in Refs. 7 and 8. For the Ce- and Ho-doped films we observe the formation of a dopant induced defect structure wherein fluorite-type precipitates tend to organized in planar arrays parallel to the *ab*-planes of the YBCO. These types of planar defects have been observed previously in excess RE-doped REBCO.[10,13] Although no definitive explanation has been proposed, such *ab*-oriented platelike structures may occur for film growth conditions where the second phase has an anisotropic surface energy with respect to the matrix. If the lower energy interface is that in the *ab* plane, such laminar nanostructures are expected. Differences in atom-by-atom subcell matchups

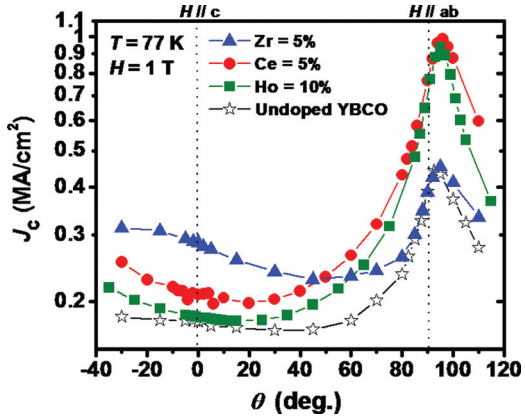

FIG. 13. (Color online) Comparison of the angular dependence of J_c (77 K, 1 T) for YBCO films doped with "optimum" levels of Ce, Ho, and Zr. Angle-selective pinning enhancement is clearly evident for different additive elements.

between the *ab*-plane versus the *c*-axis of YBCO and RE_2O_3 may yield such strain-related anisotropic surface energies, resulting in rapid lateral growth of the RE_2O_3 nuclei.[27] This defect structure leads to improved pinning (relative to undoped YBCO) for *H//ab*, with no significant pinning enhancement for *H//c* or for the "floor" J_c. In contrast, Zr doping of MOCVD YBCO generates a defect structure consisting of columnar arrays of correlated stacks of barium zirconate nanoprecipitates arranged parallel to the YBCO *c*-axis.[7,8] This columnar structure is expected to produce enhanced pinning (relative to undoped YBCO) for *H//c* but no enhancement for *H//ab*.

Taken collectively, the microstructural, XRD, Raman, and XAS results offer firm evidence that $(Y,Ce)_2O_3$ and $(Y, Ho)_2O_3$ with a fluorite lattice structure are the dominant nonsuperconducting Ce- and Ho-containing second phases, whereas, similar examinations of Zr-doped MOCVD YBCO revealed that the dominant Zr-containing phase was $BaZrO_3$-like with a perovskite type lattice structure that exhibited evidence of having some Y substitution on the Zr site.[7,8] The observation from Table II that the T_c's of the Ce, Ho, and Zr films—even the ones with the highest dopant concentrations—varied very little (~1° K) from the T_c of undoped MOCVD YBCO (made using the same procedures and equipment) provides a compelling indication that: (1) Ce and Zr do not have a significant presence in the YBCO itself, (2) Ce or Ho addition does not appear to generate any of the types of lattice disorder that lead to reductions in T_c, and (3) the Ho, which does show a clearly determined/generally expected distribution between $(Y, Ho)_2O_3$ and (Y, Ho)BCO, does not, by virtue of its presence in the REBCO, influence the T_c. In fact, the transport measurements illustrate that it takes more Ho to achieve performance levels similar to those of Ce-doped YBCO films; an observation which is consistent with these arguments.

Prior attempts to substitute Ce for RE in REBCO produced results that were somewhat contradictory. Boikov *et al.*[28] used the pulsed laser deposition (PLD) method to fabricate YBCO films with CeO_2 interlayers. They reported: (1) a decrease in T_c associated with an increasing number of CeO_2 layers, (2) XRD evidence for $BaCeO_3$ inclusions, and (3) EXAFS results that indicated the presence of Ce (IV) on Y sites in the YBCO. Kim *et al.*[29] prepared $Y_{1.2}Ce_xBa_{2.1-}Cu_{3.1}O_y$ samples $(0 < x < 0.5)$ by a solid state reaction method. They found that most of the Ce appeared in the samples as $BaCeO_3$, but that some Ce also appeared to enter the YBCO lattice with implications that the Ce resided on or otherwise influenced the Cu1 site.

Goswami *et al.*[25] reported the results of Ho additions to $YBa_2Cu_3O_7$ films produced by metal-organic deposition (MOD). Their results were comparable to ours due to the fact that the Ho appeared as (Y,Ho)BCO and as $(Y,Ho)_2O_3$ precipitates. In fact, for a film with Y/Ho = 1.0 they found that the Y/Ho ratio in the superconducting phase was 1.15. Molodyk *et al.*'s[26] study of MOCVD $Y_xHo_{1-x}Ba_2Cu_3O_7$ $(0 < x < 1)$ films showed clearly that Ho substitutes uniformly for Y as evidenced by the observation that the superconducting properties were nearly independent of the value of x. This absence of a dependence of T_c and J_c on x was attributed to the closeness of the ionic radii of Y(III) (1.019 Å) and Ho(III) (1.015 Å).

With further regard to the tendency for $(Y,Ce)_2O_3$ to form (e.g., instead of $BaCeO_3$ or CeO_2) when Ce is added to MOCVD YBCO, prior studies by Barker and Wilson[30] showed that a body centered cubic fluorite phase is stable for a wide range of Ce/Y ratios. With this in mind, the results in Fig. 7 indicate that the Ho-doped samples show a higher fluorite phase fraction than their Ce-doped counterparts. This may be due to the partial substitution of the Y site in YBCO with Ho, leading to uncertainty in the actual composition of the fluorite phase. If all of the added Ho were incorporated into YBCO, the fluorite would remain Y_2O_3 and the volume fraction calculations presented here would be correct. If instead, enough Ho is incorporated into the fluorite to increase the $(Y,Ho)_2O_3$ volume by 1%, scattering factor calculations predict that the fluorite-phase diffracted power will increase by 2.6%, since Ho has a much larger scattering factor than Y, leading to a proportional overestimate of the fluorite volume. If the 1% addition were Ce, the diffracted power would increase by only 2.2% due to the smaller Ce scattering factor.

Nevertheless, despite the relatively lower fluorite content, the 5 mol. % Ce-doped film displays better *ab*-plane pinning performance than the 5 mol. % Ho-doped film. This enhancement for the 5 mol. % Ce-doped sample (compared to the 5 mol. % Ho-doped sample) is accompanied by an increase in the amount of stacking faults associated with the RE-oxide particles and also, perhaps an increase in the amount of small secondary phase copper-containing precipitates (e.g., CuO and Ba-Cu-O). Indeed, earlier reports on RE-doped metal-organic deposited YBCO films have shown that the stacking faults (intergrowths) are largely responsible for current enhancement at *H//ab*.[31] The particles that are commonly linked to these stacking faults (and also to tilted YBCO grains) are the larger Ba-Cu-O phases,[9,32] such as the ones we typically detect in Ce- and Ho-doped films, particularly at the higher dopant concentrations, i.e., 10 mol. % Ce and 20 mol. % Ho.

We surmise from these considerations of prior work and our results on Ce- and Ho-doping of YBCO that: (1) the

method of YBCO preparation (PLD, solid state reaction, MOD, MOCVD, etc.), and (2) the process conditions (temperature, oxygen partial pressure, etc.) have a significant influence on the final phase mix and microstructure. In the case of Ce doping, the observed T_c insensitivity of Ce addition (Table II) offers compelling evidence that the Ce is not entering the YBCO lattice. The question that arises however relates to why the YBCO cation disorder increases with increasing Ce addition if the Ce is not occupying sites in the superconducting phase.

The cation disorder (C-dis) mode found in the Raman spectra shown in this work at ~530–590 cm^{-1} is caused by Raman forbidden phonons of purely tetragonal or purely orthorhombic REBCO made active by the presence of disordering effects in the REBCO lattice.[22,23,33] Some types of disorder cause a loss of inversion symmetry around the Cu1 site that leads to Raman activity of the antisymmetric O4 mode along the *c*-axis.[33] Random occupancy of metal atom positions in the REBCO lattice by dopant atoms (e.g., Ce or Ho in the present case) could produce such a disordering effect, as could the cation vacancies, anti-siting of the Y, Ba, and/or Cu atoms, or disorder in the oxygen sublattice (e.g., at the O1 position). However, another major source of such disorder occurs at the boundaries between superconductor grains and second phase precipitates, and along twist boundaries, misfit dislocations, etc. It is more likely in the case of our Ce doping results that the increase in cation disorder is related to this latter type of structural imperfection.

An earlier study reported that cation disorder in the YBCO lattice may contribute to a point-defect-type flux pinning effect that isotropically enhances self-field J_c.[23] On the other hand, Chen *et al.*[34] showed that the enhanced pinning by point-scale pinning centers may only be beneficial to J_c at low magnetic fields. It is therefore hard to establish a direct correlation between the magnitude of cation disorder and J_c at elevated magnetic fields, especially when strong precipitate pinning centers, like those previously discussed, are present. For the samples studied in this work, we attribute the pinning gain from Ce- or Ho-doping mainly to the high density of artificially introduced $(Y,Ce)_2O_3$ and $(Y,Ho)_2O_3$ nanoprecipitate arrays parallel to the *ab*-planes of the YBCO, and to the stacking faults associated with these and possibly with other secondary phase precipitates (Fig. 3) which, unlike the isotropic pinning associated with cation disorder, demonstrate a correlated pinning effect for *H*//*ab*. Therefore, for the sample types described herein, it seems desirable to maintain a low cation disorder level in order to reduce YBCO lattice deterioration.

Although the various artificial, precipitate-type pinning centers are similar in the fact that they are usually nonsuperconducting particles in the 10 nm size range, their pinning efficiency can be vastly different even at similar concentrations. The influence of nanoprecipitate size, geometry, distribution, interfacial strain state, and correlation with pinning, is a matter of great importance that is receiving considerable attention in recent literature related to REBCO-coated conductors.[35,36]

Figures 8 and 9 reveal a clear trend of increasing magnitude of cation disorder with increasing Ce or Ho. A similar observation was made in our prior study of Zr-doped MOCVD YBCO.[8] Beyond a certain level of cation disorder, the YBCO matrix suffers a deterioration of superconducting properties that compromises the beneficial pinning effects of the additive element. For the present samples, Ho addition seems to have a smaller effect on the cation disorder level, allowing up to 10 mol. % Ho to be added without inducing excessive cation disorder. This is particularly important for pinning optimizations, as the maximum pinning force is proportional to the pin density. The key for pinning optimization is to identify proper pinning dopants that transfer themselves fully into useful pinning structures rather than current-blocking clusters.

V. CONCLUSIONS

The effects of Ce and Ho additions on the electrical, microstructural, and chemical properties of MOCVD YBCO films were studied on $LaMnO_3$/IBAD-MgO templates. A combination of TEM, XRD, Raman spectroscopy, and XAS techniques was employed to ascertain variations in properties, such as texture, lattice disorder, defect structures, and phase composition/assembly with varying mole percentages of added Ce and Ho. Results were also put into perspective with respect to our previous work on Zr-doped MOCVD YBCO. We highlight the findings of this study as follows. (1) Both Ce and Ho additions result in the formation of fluorite like $(Y,Ce)_2O_3$ and $(Y,Ho)_2O_3$ nanoplatelets, respectively, in the YBCO matrix. (2) Stacking faults and antiphase boundaries emanate from these secondary precipitates. (3) As a consequence, these defect structures yield significantly enhanced J_c performance for magnetic field orientations that are near parallel to the *ab*-planes, while not much of an improvement is detected for all other field orientations. (4) Partial substitution of the Y-site in YBCO with Ho is recognized as one of the main differences between these two additives. (5) Above optimum doping concentrations (i.e., 5 mol. % Ce, 10 mol. % Ho), YBCO performance falls off sharply, due, we believe, to a combination of factors that includes increasing $(Y,Ce)_2O_3$ and $(Y,Ho)_2O_3$ particle size, increasing amounts of secondary phases (mainly CuO), misoriented YBCO grains, and decreasing YBCO volume fraction. A particularly interesting finding is the increase in the cation disorder with increasing dopant content, reaching comparable levels at the concentrations that led to optimum pinning performance. The results of this work provide an improved understanding of and correlation with the structural/chemical properties and pinning performance of MOCVD YBCO films with two metallic cation additives, one of which (Ho) substitutes freely for Y in the YBCO lattice and another (Ce) which does not appear to enter the YBCO lattice to any measureable extent.

ACKNOWLEDGMENTS

The research was sponsored by the U.S. Department of Energy, Office of Electricity Delivery and Energy Reliability, Advanced Cables and Conductors Program. Use of instrumentation at Argonne's Electron Microscopy Center, Center for Nanoscale Materials, and Advanced Photon

Source was supported by the Office of Science, Office of Basic Energy Sciences, Scientific User Facility Division. The support of this research by Venkat Selvamanickam at the University of Houston and Yimin Chen of SuperPower, Inc, are greatly appreciated.

[1]V. Selvamanickam and J. Dackow, in *2010 DOE Advanced Cables and Conductors Peer Review* (Alexandria, VA, 2010).
[2]P. Odier, A. Girard, Y. Cointe, S. Donet, Z. Yu, T. Caroff, A. Cavallaro, and A. Guibadj, 2006 BIMW: 2006 Beijing International Materials Week, Parts 1-4, **546–549**, 1855 (2007).
[3]M. Mori, T. Watanabe, N. Kashima, S. Nagaya, T. Muroga, S. Miyata, Y. Yamada, T. Izumi, and Y. Shiohara, Physica C **445**, 515 (2006).
[4]C. J. Kim, B. H. Jun, H. J. Kim, J. K. Choi, L. S. Heon, and J. Yoo, Physica C **426**, 915 (2005).
[5]V. Selvamanickam, Y. M. Chen, X. M. Xiong, Y. Y. Y. Xie, M. Martchevski, A. Rar, Y. F. Qiao, R. M. Schmidt, A. Knoll, K. P. Lenseth, and C. S. Weber, IEEE Trans. Appl. Supercond. **19**, 3225 (2009).
[6]V. A. Maroni, Am. Ceram. Soc. Bull. **86**, A29 (2007).
[7]T. Aytug, M. Paranthaman, E. D. Specht, Y. Zhang, K. Kim, Y. L. Zuev, C. Cantoni, A. Goyal, D. K. Christen, V. A. Maroni, Y. Chen, and V. Selvamanickam, Supercond. Sci.Technol. **23**, 014005 (2010).
[8]V. A. Maroni, A. J. Kropf, T. Aytug, and M. Paranthaman, Supercond. Sci.Technol. **23**, 014020 (2010).
[9]X. Y. Song, Z. J. Chen, S. I. Kim, D. M. Feldmann, D. Larbalestier, J. Reeves, Y. Y. Xie, and V. Selvamanickam, Appl. Phys. Lett. **88**, 212508 (2006).
[10]T. G. Holesinger, B. Maiorov, O. Ugurlu, L. Civale, Y. Chen, X. Xiong, Y. Xie, and V. Selvamanickam, Supercond. Sci.Technol. **22**, 045025 (2009).
[11]V. Selvamanickam, Y. Chen, J. Xie, Y. Zhang, A. Guevara, I. Kesgin, G. Majkic, and M. Martchevsky, Physica C **469**, 2037 (2009).
[12]Y. M. Chen, V. Selvamanickam, Y. F. Zhang, Y. Zuev, C. Cantoni, E. Specht, M. P. Paranthaman, T. Aytug, A. Goyal, and D. Lee, Appl. Phys. Lett. **94**, 062513 (2009).
[13]Y. Zhang, E. D. Specht, C. Cantoni, D. K. Christen, J. R. Thompson, J. W. Sinclair, A. Goyal, Y. L. Zuev, T. Aytug, M. P. Paranthaman, Y. Chen, and V. Selvamanickam, Physica C **469**, 2044 (2009).
[14]Y. Lee, H. Yamasaki, and M. Furuse, Cryogenics **50**, 459 (2010).
[15]O. V. Boytsova, S. Samoilenkov, A. Vasiliev, A. Kaul, A. Kalinov, and I. Voloshin, ECS Trans. **25**, 1185 (2009).
[16]Y. H. Kim, C. J. Kim, B. H. Jun, T. H. Sung, Y. H. Han, S. C. Han, H. J. Paik, J. S. Youn, and K. No, Physica C **469**, 1410 (2009).
[17]X. M. Xiong, S. Kim, K. Zdun, S. Sambandam, A. Rar, K. P. Lenseth, and V. Selvamanickam, IEEE Trans. Appl. Supercond. **19**, 3319 (2009).
[18]T. Aytug, M. Paranthaman, L. Heatherly, Y. Zuev, Y. Zhang, K. Kim, A. Goyal, V. A. Maroni, Y. Chen, and V. Selvamanickam, Supercond. Sci.-Technol. **22**, 015008 (2009).
[19]V. Selvamanickam, G. B. Galinski, G. Carota, J. DeFrank, C. Trautwein, P. Haldar, U. Balachandran, M. Chudzik, J. Y. Coulter, P. N. Arendt, J. R. Groves, R. F. DePaula, B. E. Newnam, and D. E. Peterson, Physica C **333**, 155 (2000).
[20]B. Warren, *X-ray Diffraction* (Dover, New York, 1990).
[21]W. R. Busing and H. A. Levy, Acta Crystallogr. **22**, 457 (1967).
[22]K. Venkataraman, R. Baurceanu, and V. A. Maroni, Appl. Spectrosc. **59**, 639 (2005).
[23]V. A. Maroni, Y. Li, D. M. Feldmann, and Q. X. Jia, J. Appl. Phys. **102**, 113909 (2007).
[24]C. Grigis, S. Schamm, and D. Dorignac, J. Mater. Res. **14**, 2732 (1999).
[25]R. Goswami, R. L. Holtz, M. W. Rupich, W. Zhang, and G. Spanos, Acta Mater. **55**, 6746 (2007).
[26]A. A. Molodyk, O. Y. Gorbenko, and A. R. Kaul, J. Alloys Compd. **251**, 303 (1997).
[27]S.A. Harrington, J. H. Durrell, B. Maiorov, H. Wang, S. C. Wimbush, A. Kursumovic, J. H. Lee, and J. L. MacManus-Driscoll, Supercond. Sci.-Technol. **22**, 022001 (2009).
[28]Y. A. Boikov, T. Claeson, D. Erts, F. Bridges, and Z. Kvitky, Phys. Rev. B **56**, 11312 (1997).
[29]C. J. Kim, K. B. Kim, S. C. Kwon, I. S. Chang, and D. Y. Won, J. Mater. Sci. Lett. **11**, 346 (1992).
[30]W. W. Barker and A. F. Wilson, J. Inorg. Nucl. Chem. **30**, 1415 (1968).
[31]W. Zhang, Y. Huang, X. Li, T. Kodenkandath, M. W. Rupich, U. Schoop, D. T. Verebelyi, C. L. H. Thieme, E. Siegal, T. G. Holesinger, B. Maiorov, L. Civale, D. J. Miller, V. A. Maroni, J. Li, P. M. Martin, E. D. Specht, A. Goyal, and M. P. Paranthaman, IEEE Trans. Appl. Supercond. **17**, 3347 (2007).
[32]D. J. Miller, V. A. Maroni, J. M. Hiller, R. E. Koritala, Y. M. Chen, J. L. R. Black, and V. Selvamanickam, IEEE Trans Appl. Supercond. **19**, 3176 (2009).
[33]V. Maroni, in High Temperature Superconductors, edited by R. Bhattacharya, M. Paranthaman (John Wiley & Sons, New York, 2010), p. 67.
[34]Z. Chen, F. Kametani, S. I. Kim, D. C. Larbalestier, H. W. Jang, K. J. Choi, and C. B. Eom, J. Appl. Phys. **103**, 043913 (2008).
[35]J. L. MacManus-Driscoll, S. A. Harrington, J. H. Durrell, G. Ercolano, H. Wang, J. H. Lee, C. F. Tsai, B. Maiorov, A. Kursumovic, and S. C. Wimbush, Supercond. Sci.Technol. **23**, 034009 (2010).
[36]Z. J. Chen, F. Kametani, A. Gurevich, and D. Larbalestier, Physica C **469**, 2021 (2009).